LETTER

Ballistic molecular transport through two–dimensional channels

A. Keerthi[1,2], A. K. Geim[1,2]*, A. Janardanan[1], A. P. Rooney[3], A. Esfandiar[2,4], S. Hu[2], S. A. Dar[1,2], I. V. Grigorieva[1], S. J. Haigh[3], F. C. Wang[1,5] & B. Radha[1,2]*

Gas permeation through nanoscale pores is ubiquitous in nature and has an important role in many technologies[1,2]. Because the pore size is typically smaller than the mean free path of gas molecules, the flow of the gas molecules is conventionally described by Knudsen theory, which assumes diffuse reflection (random-angle scattering) at confining walls[3–7]. This assumption holds surprisingly well in experiments, with only a few cases of partially specular (mirror-like) reflection known[5,8–11]. Here we report gas transport through ångström-scale channels with atomically flat walls[12,13] and show that surface scattering can be either diffuse or specular, depending on the fine details of the atomic landscape of the surface, and that quantum effects contribute to the specularity at room temperature. The channels, made from graphene or boron nitride, allow helium gas flow that is orders of magnitude faster than expected from theory. This is explained by specular surface scattering, which leads to ballistic transport and frictionless gas flow. Similar channels, but with molybdenum disulfide walls, exhibit much slower permeation that remains well described by Knudsen diffusion. We attribute the difference to the larger atomic corrugations at molybdenum disulfide surfaces, which are similar in height to the size of the atoms being transported and their de Broglie wavelength. The importance of this matter-wave contribution is corroborated by the observation of a reversed isotope effect, whereby the mass flow of hydrogen is notably higher than that of deuterium, in contrast to the relation expected for classical flows. Our results provide insights into the atomistic details of molecular permeation, which previously could be accessed only in simulations[10,14], and demonstrate the possibility of studying gas transport under controlled confinement comparable in size to the quantum-mechanical size of atoms.

Knudsen theory provides a comprehensive description of gas flow in the regime in which molecules collide mostly with confining walls rather than each other. Despite its universal adoption, it relies on certain assumptions, including fully diffusive surface scattering[3,5,7]. Several new experimental systems with nanoscale channels have recently been introduced, including carbon nanotubes[8,11] and nanoporous films made from graphene[15–19], graphene oxide[19,20] and other two-dimensional (2D) materials[21,22]. Several anomalies in gas-permeation properties have been reported, relative to expectations, which in certain cases[8,11] were difficult to reconcile within the classical theory. In particular, the observation of fast gas flows through narrow carbon nanotubes was attributed to a combination of specular and diffusive scattering[8,11]. Unfortunately, the exact dimensions and structure of these new systems are often insufficiently controlled, which makes it difficult to compare the observed behaviour with a large and growing body of molecular dynamics simulations[10,14]. The analysis is further complicated by the poorly understood effects of nanotube curvature[23] and, especially, the presence of adsorbates (such as hydrocarbons), which universally cover surfaces that are not under ultrahigh vacuum[9,24–26].

In this work, we report gas transport through ångström-scale slit-like channels with walls made from cleaved crystals of graphite, hexagonal boron nitride (h-BN) or molybdenum disulfide (MoS_2). These three materials were chosen as archetypal examples of crystals that can be exfoliated down to monolayers and provide atomically flat surfaces that are stable under ambient conditions[12]. The nanochannels were fabricated following the procedure described in Methods section 'Making 2D channels'. In brief, two thin (roughly 10–100 nm) crystals of the above materials were prepared by exfoliation to serve as bottom and top walls of a channel. A third, thinner crystal was plasma-etched to contain long narrow trenches (Fig. 1). It served as a spacer between the top and bottom walls. The three crystals were assembled on top of each other as shown in Fig. 1a, held together by van der Waals forces[12]. The slit height h was determined by the van der Waals thickness of the spacer crystal and could be chosen to be just one atomic layer up to as many as required. In all of the measurements reported here, the trench width w that defines the width of the resulting channels was about 130 nm, chosen to be sufficiently large to allow accurate measurements of a gas flow, but not large enough to allow sagging[13]. To increase the measurement accuracy, we often used many slits in parallel (typically 200), but some experiments were also done using individual channels. Their length L was defined by lithography and ranged from about 1 μm to more than 15 μm (Extended Data Fig. 1). An example of our 2D slits is shown in Fig. 1a, b, where MoS_2 was intentionally used as the building material to provide high contrast for transmission electron microscopy (TEM) imaging. This channel may be viewed as if a single atomic plane was removed from a bulk MoS_2 crystal, resulting in a pair of edge dislocations and a 2D empty space with $h \approx 6.7$ Å. We made and studied slits using different wall materials (see Methods section 'Cross-sectional imaging of 2D channels'), but used mainly graphene spacers, which allowed a slit height $h = N \times a$ in multiples of the graphene van der Waals thickness $a \approx 3.4$ Å, where N is the number of layers.

For measurements of gas transport through the 2D channels, we made devices as shown schematically in Fig. 1c. The van der Waals assembly was placed to seal a micrometre-sized opening in a silicon wafer (Extended Data Figs. 1, 3). The wafer separated two containers, one of which had a gas under variable pressure P whereas the other was a vacuum chamber equipped with a mass spectrometer. Unless otherwise stated, we used helium as a test gas. The applied pressure P was increased slowly to 200 mbar, which corresponds to the mean free path always being larger than 0.7 μm and typical Knudsen numbers of more than 10^4. Examples of the measured flow rates Q as a function of P are shown in Fig. 1d. As a reference, we made devices using the same fabrication procedures but without etching trenches in the spacer crystal or with partial trenches that did not connect the two containers. Those devices exhibited no discernable helium permeation, confirming that the 2D channels were the only pathway between the two containers. The minimal spacers were monolayer MoS_2 ($h \approx 6.7$ Å; as in Fig. 1) and bilayer graphene ($N = 2$; $h \approx 6.8$ Å).

Helium transport through our 2D channels was found to depend strongly on the wall material. In Fig. 1d we show that devices of exactly the same geometry ($h = 5a \approx 17$ Å) exhibited flow rates Q that were two

[1]School of Physics and Astronomy, University of Manchester, Manchester, UK. [2]National Graphene Institute, University of Manchester, Manchester, UK. [3]School of Materials, University of Manchester, Manchester, UK. [4]Department of Physics, Sharif University of Technology, Tehran, Iran. [5]Chinese Academy of Sciences Key Laboratory of Mechanical Behavior and Design of Materials, Department of Modern Mechanics, University of Science and Technology of China, Hefei, China. *e-mail: geim@manchester.ac.uk; radha.boya@manchester.ac.uk
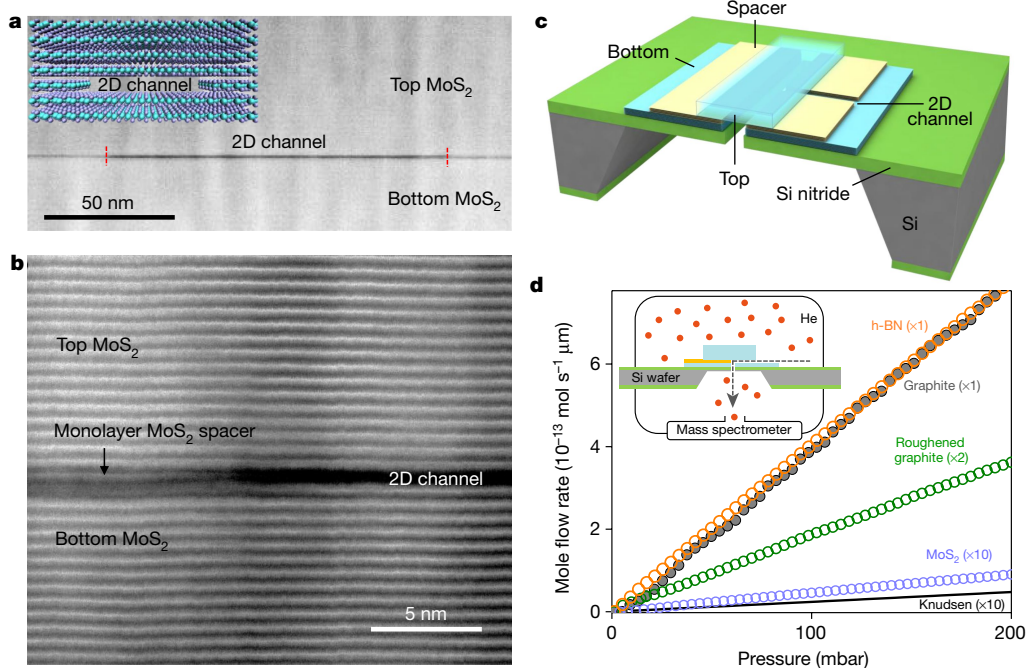
Fig. 1 | Helium gas transport through ångström-scale slits. a, Schematic (inset) and TEM micrograph (main panel) of a 2D channel assembled from MoS_2 crystals. The channel is seen in black in the main panel; for clarity, its edges are marked with red ticks. The monolayer spacer appears darker with respect to the top and bottom crystals because of different in-plane orientations. The contrast ripples running vertically are a result of the curtaining effect that occurs during ion-beam polishing[32]. Micrographs of slits made from other 2D materials are provided in Extended Data Fig. 2 and ref. [13]. **b**, High-magnification image of the channel in **a** near its left edge. Each bright horizontal line corresponds to monolayer MoS_2. **c**, Schematic of our experimental devices.

The tri-crystal assembly (cyan and yellow) covers an aperture in a silicon nitride membrane (green) prepared on top of a silicon wafer (grey). **d**, Comparison of helium permeation through 2D channels of the same height ($N = 5$), but with walls made from different crystals (as indicated by the labels). All of the devices here are single-channel, with $L = 1$–6 μm. The (mole) flow rates at room temperature (296 ± 3 K) are normalized per channel length and, for legibility, multiplied by the factors shown. The flow expected for Knudsen diffusion is shown by the solid black line close to the MoS_2 data. Inset, our measurement set-up. The arrow indicates the gas flow direction.

orders of magnitude larger for graphene and h-BN walls than for MoS_2 walls. In our case, where the mean free path of helium atoms is much larger than h, Knudsen theory predicts a mass flow rate of[5,6]

$$Q_K = \alpha P \left(\frac{m}{2\pi RT} \right)^{1/2} wh \tag{1}$$

where m is the atomic mass of the gas being transported, R is the gas constant, T is the temperature and α is the transmission coefficient. For long and narrow rectangular channels, α can be approximated as (see Methods section 'Entry effects')

$$\alpha \approx \frac{h}{L} \ln \left(\frac{4w}{h} \right) \tag{2}$$

According to these equations, and converting between mass and mole flow rates, the $N = 5$ channels in Fig. 1d should have flow rates Q shown by the solid black line. The Knudsen prediction holds (within a factor of two) only for MoS_2 walls. The other 2D slits have much higher Q. Similar disparity was observed for other values of h (see below). The large aspect ratios ($w/h \approx 100$) imply that gas molecules collide mostly with the top and bottom walls and therefore that scattering at side walls has a relatively small role, in agreement with our experimental observation that channels made using different side-wall materials but similar h exhibited similar Q (see, for example, channels in Fig. 1 and Extended Data Fig. 2b).

To quantify the observed enhancement with respect to Knudsen theory, we introduce an enhancement coefficient $K = Q/Q_K$. This allows us to summarize our findings by plotting results for more than 70 devices (Fig. 2a). Within the data scatter, the gas flow through MoS_2 channels is well described by equations (1) and (2). By contrast, all of the graphite

and h-BN devices exhibit strong enhancement ($K > 100$). There is a clear tendency for smaller K with increasing N, with K decreasing to about 10 and 3 for $N = 12$ and 25, respectively. This trend is not surprising because larger channels are expected eventually to follow the standard behaviour. The enhancement effect is so strong that graphene and h-BN slits with $h \approx 1.4$ nm exhibited a helium flux roughly ten times larger than the 9-nm slits, in contrast to equations (1) and (2), which suggest a difference by a factor of about ten but in the opposite direction.

The flow enhancement that we observe can be attributed to specular reflection of helium atoms off atomically flat walls, which should result in the breakdown of Knudsen's approximation. This possibility was first considered by Smoluchowski[4], who modified the theory by introducing the fraction f of diffusely reflected molecules. In this case, the transmission coefficient α should—in the first approximation[4,27]—be multiplied by the factor $(2 - f)/f$. Using the Smoluchowski model[4,5,10], our data yield, for example, $f \approx 0.2$ for the 4-nm graphite and h-BN channels and $f \approx 1$ for all MoS_2 devices. The largest K values in Fig. 2a suggest values of f very close to zero, that is, specular reflection. Even without taking Smoluchowski theory into account, our data for graphene channels with $N = 4$ yield practically perfect transmission. This limit ($\alpha = 1$) is plotted in Fig. 2a (dashed curve) and corresponds to the free molecular flow through an aperture of size $w \times h$. The agreement that we observe means that helium atoms pass through our long slit-like channels ballistically, without losing their momenta.

To further substantiate the observed frictionless flow, we carried out two additional experiments. First, we made graphene channels with roughened bottom walls using a short exposure to oxygen plasma (Methods section 'Making 2D channels'). This roughness suppressed
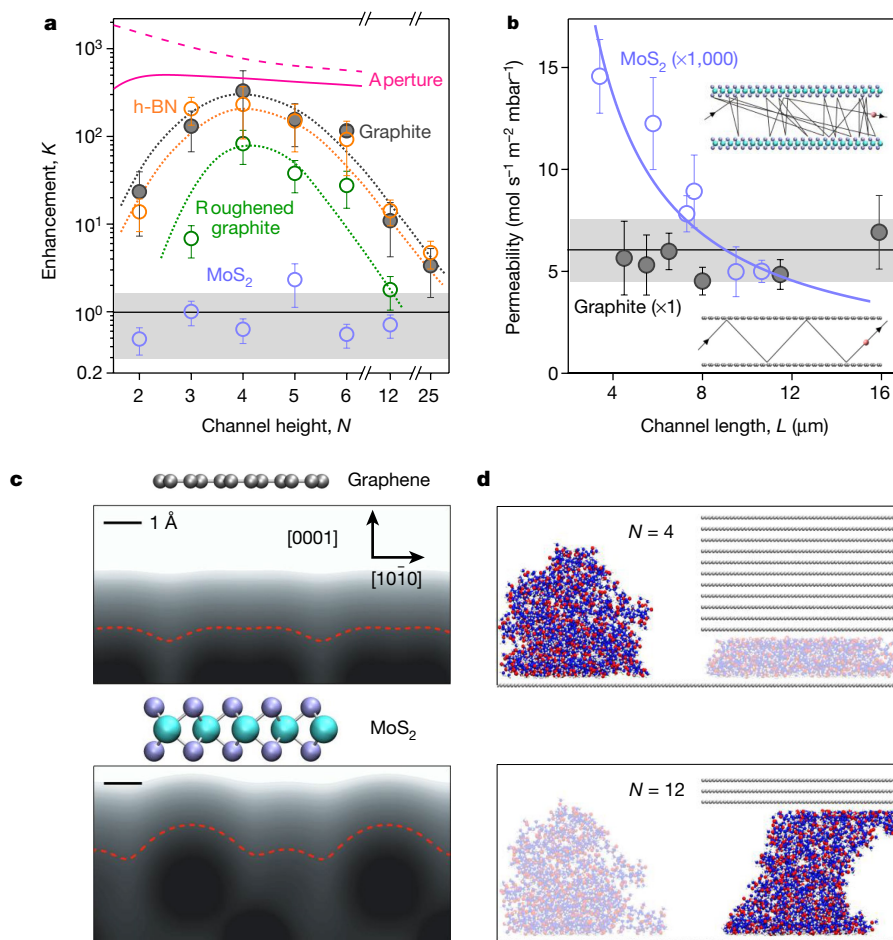
Fig. 2 | Enhanced gas flow through 2D channels. a, Enhancement factor K observed for different wall materials and channel heights (symbols). The channels could also have different L. The dotted curves are guides to the eye. MoS_2 channels exhibit no enhancement within our data scatter. The dashed pink curve indicates the K behaviour expected from equation (1) for ideal transmission. The solid pink curve is also for $\alpha = 1$, but takes into account the finite size d of helium atoms (Methods section 'Entry effects', Extended Data Fig. 7). **b**, Dependence of helium transport on L, with $N = 4$. The permeability is the flow rate divided by $P \times w \times h$. In the case of MoS_2 walls, the permeability follows the $1/L$ dependence expected for diffusive transport (the purple data are multiplied by a factor of 1,000); the purple curve is a $1/L$ fit. No length dependence is found for graphene channels, a clear signature of frictionless transport.

The insets illustrate diffusive (top) and specular (bottom) scattering. Error bars in **a** and **b** show statistical errors from our measurements, using at least two devices for each N in the case of **a**. The shaded areas in **a** and **b** indicate the standard error for the datasets shown by the purple symbols for MoS_2 in **a** and the black symbols for graphite in **b**. **c**, Intrinsic roughness of atomically flat surfaces. Grey scale, electron density near graphene and MoS_2 surfaces; red curves, depth accessible for helium atoms with thermal energies (for details, see Methods section 'Intrinsic surface roughness of 2D crystals'). **d**, Self-cleansing of 2D slits. Favourable and unfavourable positions (bright and faint, respectively) are illustrated for a polymer molecule inside slits with different N.

the helium flow by an order of magnitude, albeit insufficient to recover the Knudsen description (Figs. 1d, 2a). Non-zero specularity can be attributed to the fact that the oxygen plasma tends to etch holes in graphite so that a large portion of its surface remains flat[28]. However, the clearest evidence for ballistic transport comes from the second set of experiments, in which we used channels of the same height $h = 4a$ (strongest enhancement) but with different L. In Fig. 2b we show that the gas flow through the channels with MoS_2 walls decreases with L and exhibits the $Q \propto 1/L$ dependence prescribed by the standard theory. By contrast, for graphene slits the gas flow is independent of L, a hallmark of ballistic transport.

The considerable difference between the devices with MoS_2 and graphene or h-BN walls is surprising. Cleaved MoS_2 may not be as perfect as graphene but its surface still contains few defects[29], especially in comparison with roughened graphene. We believe that the difference arises from a finite roughness of ideal, atomically flat surfaces. In Fig. 2c we show that MoS_2 exhibits relatively strong corrugations, reaching around 1 Å in height; incoming helium atoms should therefore be able to 'see' this roughness because its scale is comparable to both the kinetic diameter ($d \approx 2.6$ Å) and de Broglie wavelength ($\lambda_B \approx 0.5$ Å) of helium

at room temperature. The former is a semi-classical notion, but, nonetheless, represents the quantum-mechanical size of the electron cloud around helium nuclei[30]. Graphene and h-BN surfaces are much flatter on this scale (Fig. 2c, Extended Data Fig. 4), suggesting more specular reflection.

The above experiments cannot distinguish between the effects of d and λ_B. To determine whether quantum effects contribute to the observed specular reflection, we compared hydrogen and deuterium permeation. These isotopes have the same d and the same interaction with the walls but different λ_B. Equation (1) suggests that Q should be a factor of $\sqrt{2}$ larger for deuterium, independently of the experimental details (such as the channel geometry or f). This benchmark dependence was validated using micrometre-sized reference apertures (Methods section 'Gas transport measurements'). By contrast, our graphene channels with $N = 4$ exhibited a flow rate Q about 30% $\pm$ 10% smaller for deuterium than for hydrogen. This finding demonstrates that matter-wave effects contribute to the specular reflection, leading to its suppression for the heavier atoms (deuterium) because they have a shorter λ_B and see an atomic landscape that is rougher than that seen by hydrogen.

Finally, we discuss the changeover from ballistic to classical (diffusive) transport, which is observed for relatively large $h \approx 4$–8 nm (Fig. 2a). We believe the underlying reason for the transition is that such large channels are no longer atomically flat, owing to hydrocarbon contamination. Cleaved surfaces are rapidly covered with various adsorbates even under cleanroom conditions[24–26]. This is particularly obvious in high-resolution TEM where only tiny areas of graphene devoid of hydrocarbons can be found[24]. However, when two atomically flat surfaces are brought together, this contamination is known to aggregate into well-separated pockets (so-called contamination bubbles), outside of which the attached surfaces become atomically clean, free of any adsorbates[12,25]. This self-cleansing is likely to start to occur at a finite separation between 2D crystals because individual polymer molecules tend to arrange themselves into clumps of a few nanometres in height (Fig. 2d, Methods section 'Self-cleansing of 2D slits'). Confining such clumps between parallel walls reduces their configurational entropy that competes with an energy gain due to adhesion (Extended Data Fig. 5). The latter is a surface effect whereas the former is determined by the volume of the clumps, which implies that the squashed clumps become energetically unfavourable at small h and should be squeezed out. Our molecular dynamics simulations (Methods section 'Self-cleansing of 2D slits') show that polymer molecules prefer to sit outside narrow channels, whereas an interior position is more favourable for larger h (Fig. 2d). With increasing N, no sharp cut-off is expected for the self-cleansing mechanism, but it should become increasingly less efficient, which would explain the observed decrease in K at large N in Fig. 2a. As for the decrease in K observed at the other end ($N = 2$ and 3), we speculate that it could be due to another size effect. The space that is not filled with electron clouds and is therefore available for molecular transport is about 6.7 Å wide, only slightly larger than $d \approx 2.6$ Å (Extended Data Fig. 6). In combination with a de Broglie wavelength of $\lambda_B \approx 0.5$ Å, which effectively increases d, this effect should decrease the number of atoms that can enter the narrow slits, especially at shallow incident angles (solid curve in Fig. 2a, Methods section 'Entry effects'). Interplay between the mechanisms that suppress molecular flow at large and small N leads to the observed dome-shaped dependence. Further theory and simulations are needed to analyse the size effects in detail.

To conclude, our work offers new understanding for many previous predictions, calculations and observations. For example, it seems to reconcile widely varying results for molecular transport through carbon nanotubes. A strongly enhanced gas flow[8,11] was reported for sub-2-nm nanotubes, whereas no such enhancement was found using wider tubes, in conceptual agreement with the transition from ballistic to diffusive transport reported here, due to the increasing role of hydrocarbon contamination in larger channels. We also note an analogy with ballistic electron transport in metallic systems. These systems can exhibit a finite electrical resistance even in the absence of electron scattering, which is known as the point contact resistance[31]. This effect is described by the Sharvin formula[31], which is equivalent to equation (1) with $\alpha = 1$ but for a charge rather than a gas flow. Ballistic effects in molecular transport have not previously been considered, even in theory; the ångström-scale channels that we have demonstrated now make this regime accessible experimentally.

Online content

Any Methods, including any statements of data availability and Nature Research reporting summaries, along with any additional references and Source Data files, are available in the online version of the paper at https://doi.org/10.1038/s41586-018-0203-2.

1. Baker, R. W. *Membrane Technology and Applications* 2nd edn (John Wiley & Sons, Chichester, 2004).
2. Lu, G. Q. & Zhao, X. S. *Nanoporous Materials: Science and Engineering* (Imperial College Press, London, 2004).
3. Knudsen, M. Die Gesetze der Molekularströmung und der inneren Reibungsströmung der Gase durch Röhren. *Ann. Phys.* **333**, 75–130 (1909).
4. v. Smoluchowski, M. Zur kinetischen Theorie der Transpiration und Diffusion verdünnter Gase. *Ann. Phys.* **338**, 1559–1570 (1910).
5. Steckelmacher, W. A review of the molecular flow conductance for systems of tubes and components and the measurement of pumping speed. *Vacuum* **16**, 561–584 (1966).
6. Livesey, R. G. in *Foundations of Vacuum Science and Technology* (ed. Lafferty, J. M.) *Ch. 2* (John Wiley & Sons, New York, 1998).
7. Lei, W., Rigozzi, M. K. & McKenzie, D. R. The physics of confined flow and its application to water leaks, water permeation and water nanoflows: a review. *Rep. Prog. Phys.* **79**, 025901 (2016).
8. Holt, J. K. et al. Fast mass transport through sub-2-nanometer carbon nanotubes. *Science* **312**, 1034–1037 (2006).
9. Agrawal, A. & Prabhu, S. V. Survey on measurement of tangential momentum accommodation coefficient. *J. Vac. Sci. Technol. A* **26**, 634–645 (2008).
10. Bhatia, S. K., Bonilla, M. R. & Nicholson, D. Molecular transport in nanopores: a theoretical perspective. *Phys. Chem. Chem. Phys.* **13**, 15350–15383 (2011).
11. Majumder, M., Chopra, N. & Hinds, B. J. Mass transport through carbon nanotube membranes in three different regimes: ionic diffusion and gas and liquid flow. *ACS Nano* **5**, 3867–3877 (2011).
12. Geim, A. K. & Grigorieva, I. V. Van der Waals heterostructures. *Nature* **499**, 419–425 (2013).
13. Radha, B. et al. Molecular transport through capillaries made with atomic-scale precision. *Nature* **538**, 222–225 (2016).
14. Zhang, W.-M., Meng, G. & Wei, X. A review on slip models for gas microflows. *Microfluid. Nanofluidics* **13**, 845–882 (2012).
15. Koenig, S. P., Wang, L., Pellegrino, J. & Bunch, J. S. Selective molecular sieving through porous graphene. *Nat. Nanotechnol.* **7**, 728–732 (2012).
16. Berry, V. Impermeability of graphene and its applications. *Carbon* **62**, 1–10 (2013).
17. Celebi, K. et al. Ultimate permeation across atomically thin porous graphene. *Science* **344**, 289–292 (2014).
18. Wang, L. et al. Molecular valves for controlling gas phase transport made from discrete ångström-sized pores in graphene. *Nat. Nanotechnol.* **10**, 785–790 (2015).
19. Kim, H. W. et al. Selective gas transport through few-layered graphene and graphene oxide membranes. *Science* **342**, 91–95 (2013).
20. Li, H. et al. Ultrathin, molecular-sieving graphene oxide membranes for selective hydrogen separation. *Science* **342**, 95–98 (2013).
21. Liu, G., Jin, W. & Xu, N. Two-dimensional-material membranes: a new family of high-performance separation membranes. *Angew. Chem. Int. Ed.* **55**, 13384–13397 (2016).
22. Wang, L. et al. Fundamental transport mechanisms, fabrication and potential applications of nanoporous atomically thin membranes. *Nat. Nanotechnol.* **12**, 509–522 (2017).
23. Falk, K. et al. Molecular origin of fast water transport in carbon nanotube membranes: superlubricity versus curvature dependent friction. *Nano Lett.* **10**, 4067–4073 (2010).
24. Gass, M. H. et al. Free-standing graphene at atomic resolution. *Nat. Nanotechnol.* **3**, 676–681 (2008).
25. Haigh, S. J. et al. Cross-sectional imaging of individual layers and buried interfaces of graphene-based heterostructures and superlattices. *Nat. Mater.* **11**, 764–767 (2012).
26. Li, Z. et al. Effect of airborne contaminants on the wettability of supported graphene and graphite. *Nat. Mater.* **12**, 925–931 (2013).
27. Arya, G., Chang, H.-C. & Maginn, E. J. Knudsen diffusivity of a hard sphere in a rough slit pore. *Phys. Rev. Lett.* **91**, 026102 (2003).
28. You, H. X., Brown, N. M. D. & Al-Assadi, K. F. Radio-frequency plasma etching of graphite with oxygen: a scanning tunnelling microscope study. *Surf. Sci.* **284**, 263–272 (1993).
29. Addou, R., Colombo, L. & Wallace, R. M. Surface defects on natural MoS2. *ACS Appl. Mater. Interfaces* **7**, 11921–11929 (2015).
30. Mehio, N., Dai, S. & Jiang, D. Quantum mechanical basis for kinetic diameters of small gaseous molecules. *J. Phys. Chem. A* **118**, 1150–1154 (2014).
31. Sharvin, Y. V. A possible method for studying Fermi surfaces. *Sov. Phys. JETP* **21**, 655–656 (1965).
32. Giannuzzi, L. A. & Stevie, F. A. (eds) *Introduction to Focused Ion Beams: Instrumentation, Theory, Techniques and Practice* (Springer, New York, 2005).

Additional information
Extended data is available for this paper at https://doi.org/10.1038/s41586-018-0203-2.
Reprints and permissions information is available at http://www.nature.com/reprints.
Correspondence and requests for materials should be addressed to A.K.G. and B.R.
Publisher's note: Springer Nature remains neutral with regard to jurisdictional claims in published maps and institutional affiliations.

METHODS

Making 2D channels. Our devices were made following the microfabrication procedures illustrated in Extended Data Fig. 1. First, a free-standing silicon nitride (SiN_x) membrane with dimensions of about $100\,\mu m \times 100\,\mu m$ was prepared, starting with the standard Si wafer covered with a 500-nm-thick layer of SiN_x. This was done using photolithography and wet etching. A rectangular hole about $3\,\mu m \times 26\,\mu m$ in size was then made in this membrane using photolithography and dry etching. Next a thin (roughly 10–30 nm) crystal of graphite, h-BN or MoS_2 was mechanically exfoliated and transferred[12,13] onto the membrane to cover the opening (Extended Data Fig. 1a). This crystal served as the bottom layer in our trilayer-crystal assembly. Following the transfer, the rectangular hole was extended into the bottom layer using the SiN_x membrane as a mask for dry etching from the back side of the Si wafer (Extended Data Fig. 1b). To this end, oxygen plasma was used for etching graphite, whereas h-BN and MoS_2 were etched in a mixture of CHF_3 and oxygen.

To make the second (spacer) layer, 2D crystals of graphene or MoS_2 were exfoliated onto an oxidized Si wafer (300 nm of SiO_2). Crystals of a chosen thickness were then etched into stripes about 130 nm wide and separated by the same distance. This was done using electron-beam lithography (polymethyl methacrylate (PMMA) with a molecular weight of 950,000 was used as a resist) and plasma etching. The PMMA mask was removed by mild sonication in acetone. The resulting stripes were transferred on top of the bottom layer as shown in Extended Data Fig. 1c, d. Next, a relatively thick (roughly 100 nm) crystal of graphite, h-BN or MoS_2 was dry-transferred[13,33] on top of the two-layer assembly so that it covered the rectangular hole and partially overlapped with the spacer stripes. After each layer transfer we annealed our assembly in 10%-hydrogen-in-argon at 300–400 °C for 3 h. The annealing step was critical for the cleanliness of the final devices, to avoid the channels becoming blocked with PMMA residue.

For the experiment that used roughened channels, the bottom graphite crystal was exposed briefly to oxygen plasma to remove approximately three layers of graphene. This was done before transferring the spacer layer. To define the length L of the final channels, a metal mask (5 nm Cr/50 nm Au) was placed by photolithography on top of the final assembly as shown in Extended Data Figs 1e, f. Dry etching through this mask not only allowed us to control L accurately, but also opened the entries of the channels if they were blocked accidentally by the thin (less than 10 nm) edges of the top crystal, which tended to sag inside the channels[13]. For single-channel devices used in some experiments (see, for example, Fig. 1d), extra nanocavities were created around the main channel (Extended Data Fig. 1d) to prevent the formation of bubbles that collect hydrocarbons and other contaminants[12,25,33] and so could block individual channels. These cavities were arranged perpendicular to the main channel (Extended Data Fig. 1d) and did not contribute to gas transport through the final devices.

Cross-sectional imaging of 2D channels. For scanning transmission electron microscopy (STEM) and high-angle annular dark-field (HAADF) imaging, we made thin cross-sectional lamellae by implementing an in situ lift-out procedure[25,34]. Lamellae were cut out perpendicular to the capillary axis by high-precision site-specific milling in Helios Nanolab DualBeam 660, which incorporates scanning electron microscope and focused ion-beam columns. Platinum was deposited using the ion beam to weld the lamella to a micromanipulator, which was then lifted from the substrate. Once transferred to a specialist OmniProbe TEM grid, the lamella foil was thinned to less than 100 nm and then polished further to electron transparency, using 5-kV and subsequently 2-kV ion milling. High-resolution STEM and HAADF images were acquired in an aberration-corrected microscope (FEI Titan G2 80-200 kV) using a probe convergence angle of 21 mrad, a HAADF inner angle of 48 mrad and a probe current of about 70 pA. To ensure that the electron beam was parallel to the 2D channels, it was aligned using the relevant Kikuchi bands of the silicon substrate and the assembled 2D crystals.

Gas transport measurements. Gas permeation through our 2D slits was studied in the steady-state flow regime using the set-up shown in Extended Data Fig. 3a. The SiN_x/Si wafer containing a capillary device was sealed using O-rings to separate two oil-free vacuum chambers. Standard vacuum components were used to make the two-chamber assembly sketched in Extended Data Fig. 3a. The chambers were evacuated before every experimental run. One of the chambers was equipped with an electrically controlled dosing valve that provided the pressure P inside, which was monitored by a pressure gauge. The applied pressure was varied slowly to avoid any time delays or hysteresis. The top (entry) side of our devices was facing this chamber (Extended Data Fig. 3a). The devices were sufficiently robust to withstand P up to 2 bar. The other chamber was maintained at a pressure of around 10^{-6} bar, and connected to a mass spectrometer. For measurements of helium, hydrogen and deuterium flows, we used a calibrated helium-leak detector (INFICON UL200) as the mass spectrometer. The leak detector measures the flow rates in units of mbar l s^{-1}, which are straightforward to convert into units of mol s^{-1} using the ideal-gas equation. All the measure-

ments were done at room temperature ($T = 296 \pm 3$ K), as measured by a probe mounted close to the device.

The measurement set-up was checked thoroughly for possible leaks using control devices that were prepared following the same fabrication procedures but without complete 2D channels (see the main text). These control devices exhibited no discernible He leak, which demonstrates that the 2D channels were the only possible permeation path for the gases tested. To assure quantitative accuracy of our measurements, we also prepared reference devices containing round apertures made in SiN_x membranes and tested their conductance with respect to helium. The measured flow values were indistinguishable from those given by the Knudsen equation (Extended Data Fig. 3b). For the other gases, the apertures were used to calibrate the sensitivity of our mass spectrometer and to measure the isotope effect, in which the mass flow of deuterium was observed to be a factor of $\sqrt{2}$ higher than that of hydrogen, as required by equation (1).

Intrinsic surface roughness of 2D crystals. To compare the flatness of different 2D crystals that served as the walls of the slits, we used density functional theory (DFT) to calculate near-surface electron-density profiles. The results (Extended Data Fig. 4) illustrate that graphene and h-BN are atomically flatter than MoS_2, as is generally expected. For further analysis of the surface roughness, we use the criterion of the so-called thermal exclusion surface[35]. This criterion suggests that He atoms effectively 'feel' the surface at a critical density of about 0.03 electron per Å^3. Incident atoms with a kinetic energy equivalent to their thermal energy (298 K) cannot penetrate beyond this isosurface, shown by the red curves in Extended Data Fig. 4. The DFT analysis was carried out using the CP2K program[36] and the PBE exchange-correlation functional[37]. The energy cut-off for plane-wave expansions was set at 600 Ry. Gaussian basis sets for the double-zeta valence-polarized (DZVP) quality[38] and Goedecker–Teter–Hutter pseudopotentials[39] were used in the calculations. Periodic boundary conditions were applied and the vacuum region was set to have a thickness of 40 Å. The electron-density contours were analysed using Multiwfn[40].

We also carried out molecular dynamics (MD) simulations in an attempt to explain the substantial difference in molecular transport through MoS_2 and graphite channels that we observed. To this end, we constructed nanochannels with potential-energy surfaces obtained using the classical force-field parameters[41]. These surfaces are qualitatively similar to the DFT surfaces shown in Extended Data Fig. 4. The nanochannels connect two reservoirs, one of which was maintained at a pressure of 200 mbar by adjusting the number of helium atoms inside. The other was kept empty to model gas transport driven by a pressure gradient. The gas flow through graphite channels was notably higher than that through the MoS_2 channels with rougher walls, as expected. However, graphite and MoS_2 channels both exhibited a finite f and a clear dependence of the helium flux on L (that is, no ballistic transport could be seen in these MD simulations even for graphite walls), in contrast to the experiment. This indicates limitations of classical MD simulations in describing specular surface scattering or, at least, insufficient knowledge of the details of the interaction of helium with atomically flat surfaces. Moreover, our experiments with hydrogen isotopes show that not only the interaction but also the molecular mass are important for allowing perfect specular reflection, which indicates a contribution from quantum effects, as discussed in the main text. Accordingly, we limited our efforts to explain the results using classical MD analysis.

Self-cleansing of 2D slits. Self-cleansing[12,13,25] of interfaces during van der Waals assembly has been studied extensively over the past five years. As argued in the main text, similar self-cleansing processes should take place if two atomically flat surfaces are in direct contact or at finite separation. To model this, we take PMMA on graphene as an archetypal example of a poorly mobile adsorbate that is often found on graphene and other surfaces[24–26]. For a PMMA molecule confined inside an ångström-scale slit, the total free energy has two main contributions: adhesion energy with the two walls and configurational entropy. The former tends to keep PMMA inside whereas the latter increases the total energy if PMMA molecules are flattened and, therefore, pushes them out. For strong confinement (small h), the configurational entropy may become dominant and PMMA is squeezed out, which leads experimentally to the formation of contamination bubbles[25]. It is difficult to model the whole squeezing process in MD simulations because of the long timescales that are required for self-cleansing (as witnessed by the necessity of thermal annealing to clean the van der Waals heterostructures); MD analysis typically allows only simulations that correspond to less than 1 ms. In our simulations over such timescales, we saw creep of heavy hydrocarbons, but not their complete removal from the simulated nanoslits.

To avoid the timescale problem, we used metadynamics algorithms[42] to calculate the potential of mean force, which can be regarded as a spatial free-energy profile. Also, relatively small PMMA molecules with a molecular weight M of 40,000 were simulated for computational reasons, because the results are not expected to depend on M (see below). The positions of the centre of mass for such

PMMA molecules along both relevant directions (parallel (X) and perpendicular (Z) to axis of the slit) were chosen as two variables (Extended Data Fig. 5a). Parameters from OPLS forcefield[41] were used to describe the interactions among constituent atoms of the PMMA–graphene system, which include bond, angle, dihedral, improper and non-bonded (electrostatics and Lennard–Jones) interactions. Parameters for non-bonded Lennard–Jones interactions were obtained using the Lorentz–Berthelot mixing rules. The PMMA molecule was first placed on top of a graphene sheet and MD simulations were run in canonical ensembles for 10 ns with a time step of 1 fs, to reach the equilibrium at 298 K. Then, metadynamics simulations were performed for at least 300 ns. All of the calculations were carried out using LAMMPS[43].

As an example, in Extended Data Fig. 5 we show our results for two graphene capillaries with $N = 4$ and $N = 12$, which correspond to channel heights of $h \approx 13.6$ Å and $h \approx 40.8$ Å, respectively. For $N = 4$, the PMMA molecule exhibits a higher-energy state inside the capillary than outside (Extended Data Fig. 5b). Therefore, PMMA tends to be squeezed outside or, at least, move to the edge of the entrance, as also illustrated in Fig. 2d. By contrast, the free energy of PMMA is lower inside than outside the taller capillary, as shown in Extended Data Fig. 5c and Fig. 2d.

From another perspective, the height of an adsorbed polymer molecule can be estimated as $H \approx b/\delta$, where b is the Kuhn length (for PMMA, $b = 1.7$ nm)[44] and δ describes the ratio of the adhesion energy of a monomer to its thermal energy[44]. Our MD simulations for graphene yield $\delta \approx 0.3$ at 298 K and, hence, $H \approx 5.7$ nm. This is the standard estimate, which suggests that the height of adsorbed polymer clumps should not depend on their molecular weight. To verify this assumption, we carried out MD simulations for PMMA on graphene with $M = 10,000–200,000$. The apparent height H of the clumps was then calculated as an average over 10 ns. The results (Extended Data Fig. 6) confirm that the H values of adsorbed PMMA remain practically constant for $M \geq 40,000$. The value of $H \approx 4.0$ nm that we found is smaller but in reasonable agreement with estimate from theory (above). For lighter PMMA molecules, H tends to decrease to 2–3 nm, which is not surprising because the statistical chain model is expected to be valid only for long polymers.

The values of H that we obtained suggest that PMMA contaminants could be squeezed out of our 2D channels with h smaller than about 4.0 nm ($N \approx 12$), in (only) qualitative agreement with the experiment and simulations in Extended Data Fig. 5; the apparent height of polymer clumps may be not the best parameter to describe self-cleansing. Another possible measure of the height of PMMA molecules is their radius of gyration R_g. Its perpendicular component $R_{g\perp}$ provides a sense of height and so we can define the gyration height as $H_g = 2R_{g\perp}$. For self-cleansing, this parameter seems more meaningful than H because $R_{g\perp}$ refers to the size of a polymer coil[44] and therefore implies a direct connection to configuration entropy. We find that H_g for PMMA contamination is about 1.5–2 nm for large M (Extended Data Fig. 6). This value matches closely the results of Extended Data Fig. 5, and our experimental data indicate the onset of self-cleansing at similar h (Fig. 2d).

Entry effects. The Knudsen flow rate through a channel with cross-section $w \times h$ is given by equation (1). For 2D channels ($h \ll w < L$) and in the Knudsen regime, α is[6]

$$\alpha = \frac{h}{L}\left\{\frac{\ln[h/w + \sqrt{1 + (h/w)^2}]}{h/w} + \ln\left[\frac{1 + \sqrt{1 + (h/w)^2}}{h/w}\right] \right.$$
$$\left. + \frac{1 + (h/w)^3 - [1 + (h/w)^2]^{3/2}}{3(h/w)^2}\right\} \tag{3}$$

which can be approximated as[6]

$$\alpha \approx \frac{16}{3\pi^{3/2}}\frac{h}{L}\ln\left(\frac{4w}{h} + \frac{3h}{4w}\right) \approx 0.958\frac{h}{L}\ln\left(\frac{4w}{h} + \frac{3h}{4w}\right) \tag{4}$$

This expression can be simplified further to equation (2).

The Smoluchowski correction[4–6] to equations (1), (3) and (4) can be modified to make these equations applicable also in the limit of zero f, where the factor $(2 - f)/f$ diverges, resulting in infinite Q. To this end, the flow resistance caused by the entry aperture should be taken into account and, in the first approximation[10], added as a series flow resistance[5,6]. The maximum Q is then given by equation (1) with $\alpha \equiv 1$, which correspond to perfect ballistic transport. For such transport, the enhancement coefficient is

$$K = \frac{Q(\alpha = 1)}{Q(\alpha)} \approx \frac{L}{h\ln(4w/h)}$$

shown as the dashed magenta curve in Fig. 2a. This analysis ignores the finite size d of transported gas molecules.

Now let us take into account that in our experiments h is comparable with d. In the semi-classical description (ignoring the finite de Broglie wavelength), doing so implies that molecules incident sufficiently away from the centre of the channel are unable to enter it. For incidence along the channel axis ($\theta = 0$), the effective channel width h^* is reduced from h to $h - d$ (Extended Data Fig. 7). For molecules with a non-zero incidence angle θ, the effective entry width is reduced further to $h^*(\theta) = h - d/\cos\theta$. As an estimate, we may, for example, choose 45° as an 'average' incidence angle, which yields $h^* = h - \beta d \approx h - \sqrt{2}\,d$, but the coefficient β generally depends on both d and h (see below).

Taking into account the entry effect, fully ballistic transport should provide a gas flow rate of

$$Q^* = P\left(\frac{m}{2\pi RT}\right)^{1/2}wh^* \tag{5}$$

whereas the enhancement plotted in Fig. 2 (dashed curve) was calculated for $d \equiv 0$. According to equation (5), the maximum possible enhancement coefficient K^*, which takes into account both ballistic transport ($\alpha \equiv 1$) and the entry effect ($d \neq 0$) is smaller:

$$K^* = \frac{Q^*}{Q(\alpha)} = \frac{h^*}{h}K = \left(1 - \frac{d}{h}\beta\right)K \tag{6}$$

To estimate β more accurately, we consider contributions from all angles θ. Incident atoms effectively 'see' only a projection of the channel opening, $h\cos\theta$. If the projected opening is smaller than d (that is, if $h^*(\theta) \leq 0$), then the atoms hit one of the edges of the aperture. Let us assume in the first approximation that all such scattered atoms are scattered away rather than guided inside the slits. This means that, when integrating, we need to exclude the trajectories that are above the critical angle $\theta_c = \arccos(d/h)$ because they do not contribute to Q^*. This yields

$$K^* = \frac{K}{\pi}\int_{-\pi/2}^{\pi/2}1 - \frac{d}{h\cos\theta}\mathrm{d}\theta \tag{7}$$

where the averaging is carried out over all incident angles $[-\pi/2, \pi/2]$ and the integrand is set to zero for $|\theta| \geq |\theta_c|$. We can then re-write equations (6) and (7) using the average coefficient

$$\langle\beta\rangle = \frac{h}{d}\left(1 - \frac{2\theta_c}{\pi}\right) + \frac{2}{\pi}\int_0^{\theta_c}\frac{\mathrm{d}\theta}{\cos\theta}$$

Noting that

$$\int\frac{\mathrm{d}\theta}{\cos\theta} = \ln\left(\frac{1 + \sin\theta}{\cos\theta}\right)$$

we obtain

$$\langle\beta\rangle = \frac{h}{d}\left(1 - \frac{2\theta_c}{\pi}\right) + \frac{2}{\pi}\ln\left(\frac{1 + \sin\theta_c}{\cos\theta_c}\right)$$

For the He-atom diameter of 2.6 Å, we find the K^* dependence shown by the solid magenta curve in Fig. 2a. Our graphene channels with $N = 4$ exhibit the maximal enhancement, and its value agrees well with the calculated maximum possible K^*. This again indicates frictionless helium flow. The finite-size effect is expected to be enhanced by the diffraction of de Broglie waves at the entry apertures (for helium, $\lambda_B \approx 0.5$ Å), which should lead to further reductions in K^* for the smallest N. We do not expect the quantum correction to be excessively large and so we ignore the effect in this analysis.

Data availability. The data shown in the figures and that support the findings of this study are available from the corresponding authors on reasonable request.

33. Esfandiar, A. et al. Size effect in ion transport through angstrom-scale slits. *Science* **358**, 511–513 (2017).
34. Schaffer, M., Schaffer, B. & Ramasse, Q. Sample preparation for atomic-resolution STEM at low voltages by FIB. *Ultramicroscopy* **114**, 62–71 (2012).
35. Bentley, J. Electron density as a descriptor of thermal molecular size. *J. Phys. Chem. A* **104**, 9630–9635 (2000).
36. VandeVondele, J. et al. Quickstep: fast and accurate density functional calculations using a mixed Gaussian and plane waves approach. *Comput. Phys. Commun.* **167**, 103–128 (2005).
37. Perdew, J. P., Burke, K. & Ernzerhof, M. Generalized gradient approximation made simple. *Phys. Rev. Lett.* **77**, 3865–3868 (1996).

38. VandeVondele, J. & Hutter, J. Gaussian basis sets for accurate calculations on mole-cular systems in gas and condensed phases. *J. Chem. Phys.* **127**, 114105 (2007).
39. Goedecker, S., Teter, M. & Hutter, J. Separable dual-space Gaussian pseudopotentials. *Phys. Rev. B* **54**, 1703–1710 (1996).
40. Lu, T. & Chen, F. Multiwfn: a multifunctional wavefunction analyzer. *J. Comput. Chem.* **33**, 580–592 (2012).
41. Jorgensen, W. L., Maxwell, D. S. & Tirado-Rives, J. Development and testing of the OPLS all-atom force field on conformational energetics and properties of organic liquids. *J. Am. Chem. Soc.* **118**, 11225–11236 (1996).
42. Laio, A. & Parrinello, M. Escaping free-energy minima. *Proc. Natl Acad. Sci. USA* **99**, 12562–12566 (2002).
43. Plimpton, S. Fast parallel algorithms for short-range molecular dynamics. *J. Comput. Phys.* **117**, 1–19 (1995).
44. Rubinstein, M. & Colby, R. H. *Polymer Physics* Ch. 2, 3 (Oxford Univ. Press, Oxford, 2003).
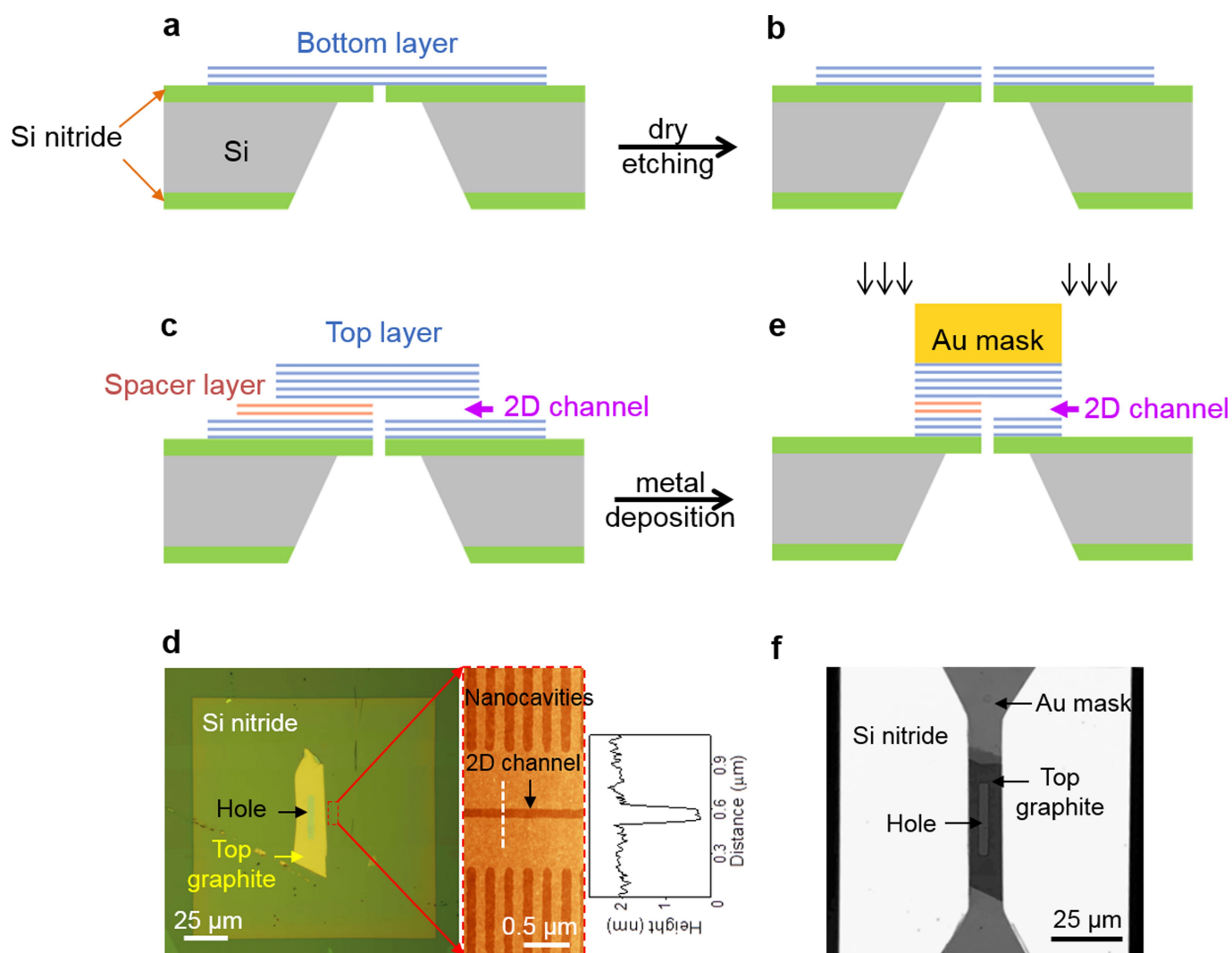
Extended Data Fig. 1 | Fabrication procedures. a, Thin crystal was transferred to cover an opening in a SiN_x membrane. **b**, The opening is extended through the bottom crystal. **c**, Spacer stripes were deposited on top of the bottom layer and etched from the back side. The top crystal is then transferred on top to fully cover the rectangular opening. **d**, Left, optical image of a single-channel capillary device made entirely from graphite; $N = 5$. The SiN_x/Si wafer is seen in dark green; the SiN_x membrane appears as a light-green square; the top graphite layer shows up in bright yellow; and the rectangular opening (lighter green) is indicated by the black arrow. Centre, atomic force micrograph near the channel entry, where the top graphite does not cover the spacer layer (the scan area is shown by the red contour). The height profile taken along the dotted white line is shown on the right, indicating $h \approx 1.7 \pm 0.1$ nm. The side cavities perpendicular to the 2D channel were made to prevent contamination bubbles[25] across the main channel. **e**, A gold mask is placed on top of the trilayer assembly for final etching, to define L and to unblock the channel entry. **f**, Optical image of the final capillary device in the transmission mode. The SiN_x membrane is fully transparent (bright). The Au mask is partially transparent, and both the top graphite and the rectangular hole in SiN_x can be seen underneath the Au, as indicated by the arrows.
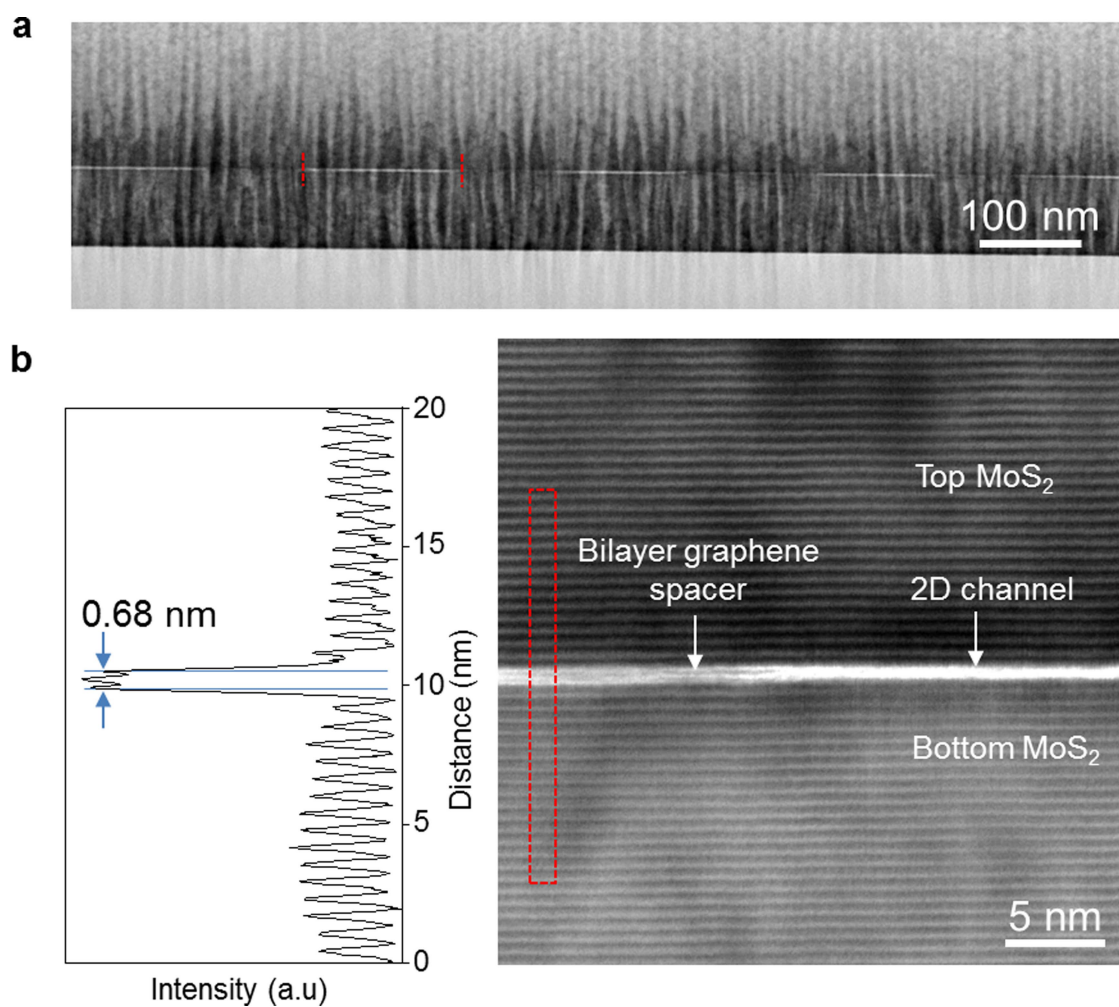
Extended Data Fig. 2 | Visualization of 2D channels. a, Array of 2D slits made entirely from MoS₂, as imaged in bright-field STEM. For guidance, the edges of one of the channels are indicated by red marks. The vertical stripes are from the curtaining effect caused by ion milling[32]. **b**, High-magnification STEM image of a 2D channel with the top and bottom walls made from MoS₂ and bilayer graphene as the spacer (right panel). The channel is white in the bright-field image, and atomic layers of MoS₂ can be seen as dark lines running parallel to the channel. The left panel shows a contrast profile across the region indicated by the red rectangle. Cross-sectional images of 2D slits made entirely from graphite crystals can be found in ref. [13].
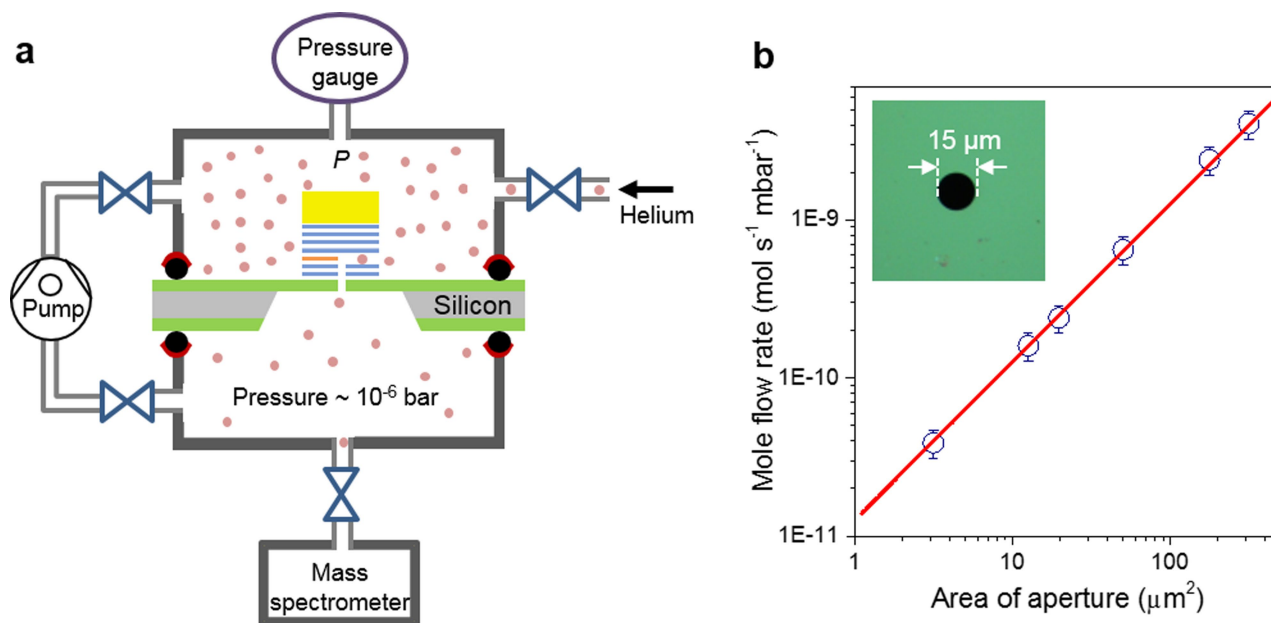
Extended Data Fig. 3 | Helium permeation measurements. a, Schematic of our experimental set-up. **b**, Helium flow through round apertures of various diameters as measured by our He-leak detector (symbols). Red line, expected Knudsen flow through these apertures (no fitting parameters). Inset, optical image of one of the apertures. The error bars are from measurements using different devices.
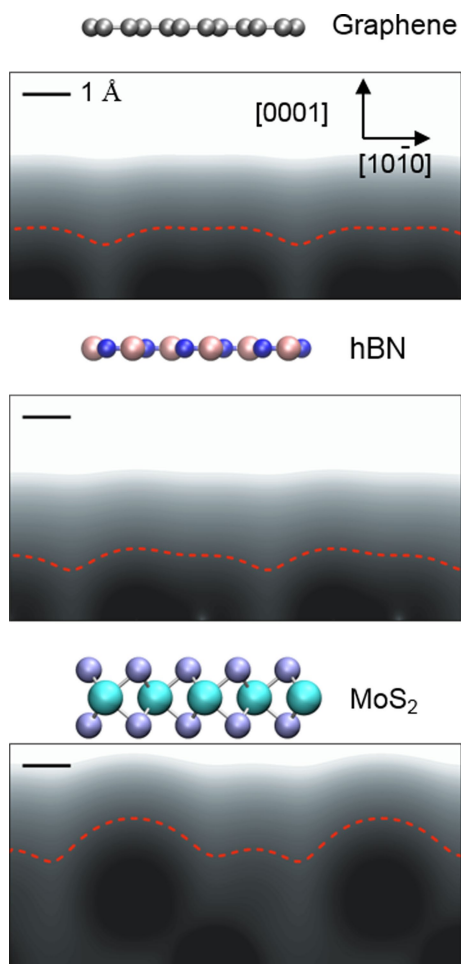
Extended Data Fig. 4 | Intrinsic roughness of atomically flat surfaces.
Electron-density profiles near graphite, h-BN and MoS_2 surfaces are shown. Schematics of the atomic structures are shown on top. The red curves indicate the thermal exclusion surfaces.
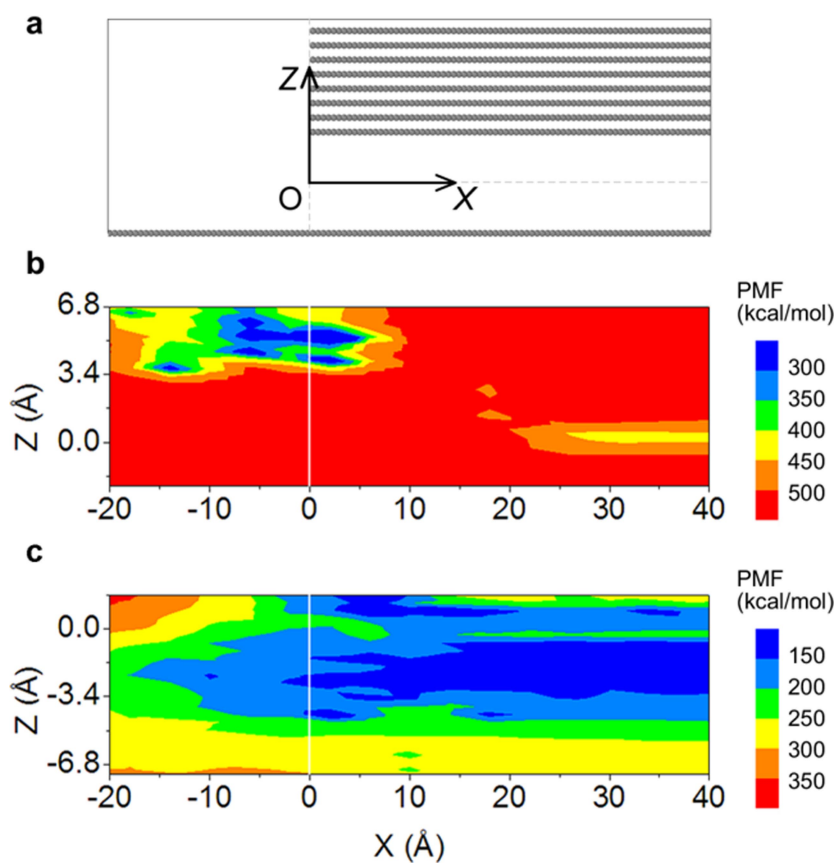
Extended Data Fig. 5 | MD simulations for a heavy polymer molecule inside ångström-scale channels. a, Sketch of our simulation set-up. **b, c**, Energy of a PMMA molecule ($M = 40,000$) for slits with $N = 4$ (**b**) and $N = 12$ (**c**). The axes show the position of the centre of mass with respect to the entrance edge. The origin of the axes is shown in **a**. The colour scales to the right show the relative free energy (potential of mean force, PMF).
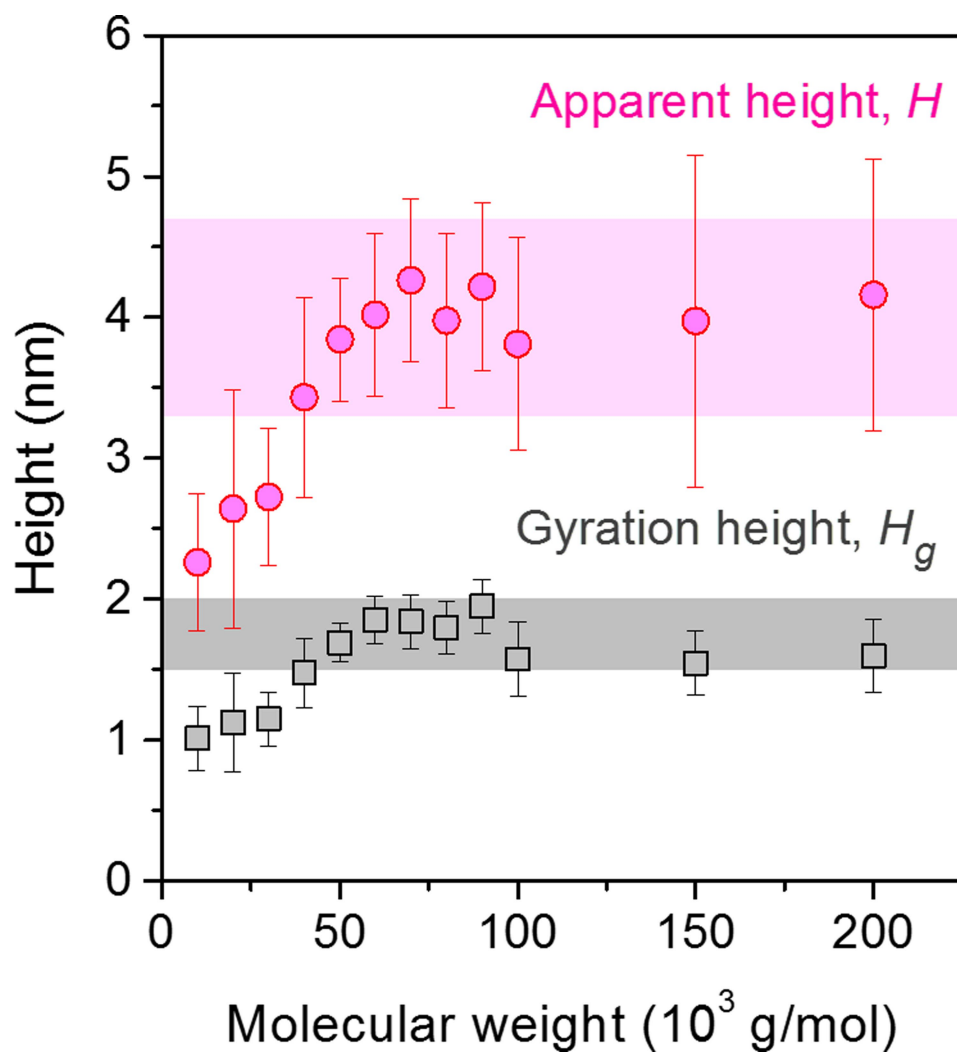
Extended Data Fig. 6 | Height of absorbed PMMA. MD results are shown for the apparent (circles) and gyration (squares) heights of PMMA on graphene. The shaded areas indicate the standard errors using the data for $M \geq 40,000$. Error bars show the standard error from our simulation runs lasting 10 ns.
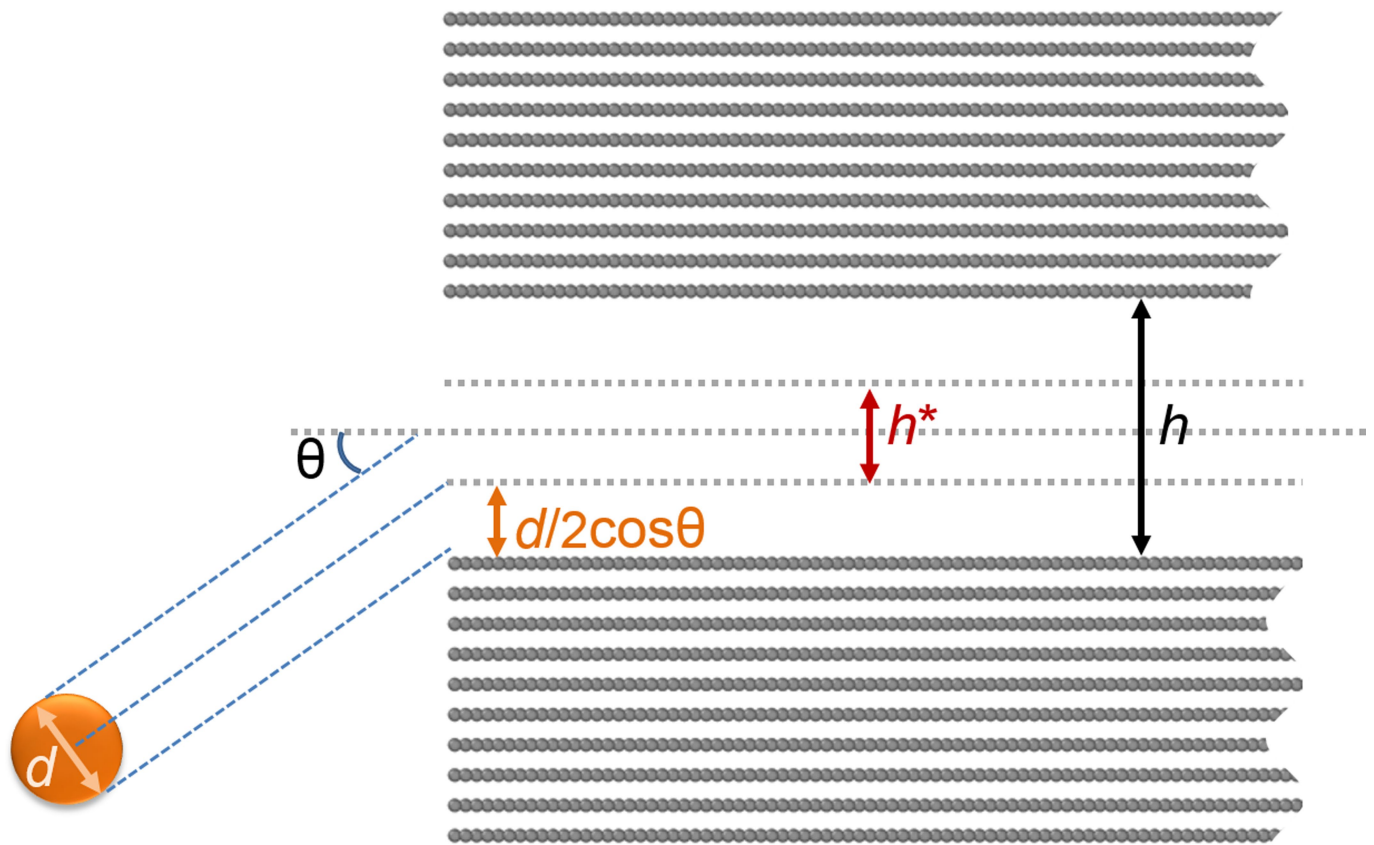
Extended Data Fig. 7 | Finite-size entry effect. If an incident atom of diameter d hits one of the edges of the channel, it can be reflected. To avoid this, the centre trajectory should be $d/(2\cos\theta)$ away from the edge, effectively reducing the entry aperture to $h^*(\theta) = h - d/\cos\theta$.